Available online at www.sciencedirect.com

jmr&t Journal of Materials Research and Technology

journal homepage: www.elsevier.com/locate/jmrt

Original Article

Study and characterization of γ-ray doses dependent properties of $CuPbI_3$ perovskite thin films

S. Aldawood [a,**], Wejdan M. Bannoob [a], M.S. AlGarawi [a], Turki S. Alkhuraiji [b], Yazeed Alashban [c], Nasser Shubayr [d], Syed Mansoor Ali [a,*]

[a] Department of Physics and Astronomy, College of Science, King Saud University, P.O. BOX 2455, Riyadh, 11451, Saudi Arabia

[b] King Abdulaziz City for Science & Technology (KACST), Nuclear Science Research Institute (NSRI), Directorate of International Cooperation (DIC), P.O. Box 6086, Riyadh, 11442, Saudi Arabia

[c] Radiological Sciences Department, College of Applied Medical Sciences, King Saud University, Riyadh, 11451, Saudi Arabia

[d] Diagnostic Radiology Department, Medical Research Center, College of Applied Medical Sciences, Jazan University, Jazan, Saudi Arabia

ARTICLE INFO

Article history:
Received 23 March 2021
Accepted 11 June 2021
Available online 24 June 2021

Keywords:
$CuPbI_3$ perovskite thin films
γ-ray's irradiation
XRD
Optical properties
Photoluminescence
Impedance spectroscopy

ABSTRACT

The impact of γ-ray on the halide perovskite ($CuPbI_3$) thin film has been investigated in this work. Nanocrystalline and homogeneous $CuPbI_3$ material was effectively deposited on a glass substrate using spin coating method. The thin film, which has a thickness of approximately 227 nm, was exposed to γ-ray's source (Co^{60} with a dose rate of 7.328 kGy/h) in the range of 0–75 kGy. Then the structural, morphological, electrical and optical properties of $CuPbI_3$ thin films were studied before and after being irradiated. X-ray diffraction (XRD) analysis confirmed the hexagonal phase structure, and the crystalline size decreased from 42 to 16 nm with increasing crystallinity up to 50 kGy. Field emission scanning electron microscopy (FESEM) revealed that the grain size (33-23 nm) and surface of thin films were significantly affected by γ-ray's doses variation. The optical transmission and reflectance of $CuPbI_3$ thin films were studied by means of their response to incident γ-rays. The estimated band gap (E_g) slightly increased from 2.23 to 2.3 eV with increasing γ-rays dose from 0 to 50 kGy and then deceased afterward. Other optical parameters, such as Urbach energy, extinction coefficients, refractive index, optical density and dielectric constants, were determined before and after γ-ray's exposure. Photoluminescence (PL) spectra depict the transition peak at 620.35 nm and the structural defect peak at 606.3 nm. The intensity of the PL peaks could depend on the γ-rays dose with respect to the as-deposited thin films. Impedance spectroscopy of all samples revealed that the grain boundary resistance gradually reduced with increasing γ-ray's dose. This study concludes

* Corresponding author.
** Corresponding author.
E-mail addresses: sdawood@ksu.edu.sa (S. Aldawood), Symali@ksu.edu.sa (S.M. Ali).

https://doi.org/10.1016/j.jmrt.2021.06.034

that the incident γ-rays play a main role in properties of the $CuPbI_3$ thin film, which is favorable for sensing/detecting applications of γ-ray's.

1. Introduction

Halide perovskite materials have aroused extensive attention for the recent extension of their technical capabilities in optoelectronic applications, particularly for radiation sensors. Due to their unique possessions of a high Z value, large stopping power, very low deep defects, high product mobility and lifetime (μτ) and easy low-cost solution synthesis, they are appropriate materials for the next generation of high-energy radiation detection [1–9]. The sensing of high-energy radiation can be applied via two methods: direct and indirect [10]. In the direct sensing of radiation, the interaction of high-energy photons with materials can directly generates a pair of charges and separated by electrodes. In indirect sensing, the high-energy radiation initially changes into light by scintillating materials and then transforms into an electronic source by a photosensor. Accordingly, the progress of radiation detector technologies that associate with better efficiency with lower-cost, large-scale, and have the capability for calibration, could cover the approach to new techniques with several assistances to humanity [11].

Compared to organic halide perovskites, inorganic halide perovskite materials are good candidates for radiation detection applications because of their extraordinary optoelectronic properties, detection efficiency, more effective atomic number and high stability [12–15]. Wu et al. reported novel 0D Cs_4EuX_6 (X = Br, I) perovskite materials with superior performance for γ-rays spectroscopy [16]. Hany et al. investigated the optical and electrical properties of $TlPbI_3$ using UV–Vis-IR spectroscopy and cathodoluminescence and current–voltage characteristics [17]. He et al. studied a $CsPbBr_3$ inorganic perovskite for the detection of γ-rays with ^{57}Co and ^{137}Cs [18]. Among the inorganic perovskites, $CuPbI_3$ has a promising electronic structure with an energy bandgap of ~ 2.1 eV, high cost-effectiveness, long-term stability due to the absence of organic molecules, high Z compounds, abundance and solution base synthesis [19]. We are initiating our research on $CuPbI_3$ thin films by studying their structural, optical and electrical properties under the influence of different γ-ray's doses to investigate the potential dosimetric and detection properties of this material.

In recent times, attention has been increased to the influence of radiation on thin film semiconductor properties [20,21]. The effects of irradiation on nanostructure materials can provide an induced effect on the properties of thin films for numerous technological applications, and calibration of these impacts with dose can be used for radiation sensor materials [22,23]. This alteration is dependent on the irradiation dosage and sensitivity of the solid films [23]. However, the change in the structural, optical and electrical properties and change mechanism with different γ-rays exposure doses have not been investigated in detail for novel $CuPbI_3$ perovskite thin films. Previously, most research studies indicated that irradiation influences the properties of oxide or chalcogenide thin films. Furthermore, the novelty of this work lies in analyzing the impact of γ-ray's irradiation at various dose levels. Perovskite thin films are nanostructured materials that lead to a good understanding of the γ-ray's interaction effect properties. To investigate whether there will be any structural, optical and electrical modification in the $CuPbI_3$ perovskite thin films due γ-ray's irradiation, all samples were examined using characteristics, such as structural, morphological, optical and electrical measurements. To the best of our knowledge, no earlier investigation on the physical properties of γ-ray's irradiated $CuPbI_3$ thin films has been achieved previously. This work will deliver new insights to the research community on γ-ray's irradiation irradiated thin films for sensing application.

2. Materials and methods

2.1. Deposition of $CuPbI_3$ thin films

CuI thin film nanoparticles were synthesized by an in situ hydrothermal method. Two precursor solutions were prepared of 0.25 M $CuSO_4 \cdot 5H_2O$ and 0.25 M KI solution in double distilled water (DDW) and stirred for 1 h. The prepared solutions were stirrered for 30 min at 70 °C and transferred into a 50-mL Teflon autoclave. The autoclave was kept at 180 °C for 2 h and cooled. The resulting solution was centrifuged and washed with DDW and ethanol. Furthermore, the CuI nanoparticles were sintered for 30 min at 100 °C.

Two compositions of 0.2 M of lead nitrate [$Pb(NO_3)_2$] and 0.4 M potassium iodide (KI) was used as the starting material in DDW. Both solutions were stirred at 70 °C for 2 h. The yellowish-color solutions were maintained in a 50-mL Teflon-lined autoclave at 180 °C for 2 h, and naturally cooled down at room temperature. Finally, it was washed with ethanol and dehydrated.

Before deposition on a glass substrate, they were cleaned with cleansing agent, DI water and ethanol. First, 1 M of prepared PbI_2 solution in DMF was coated on cleaned substrate by spin coating at 3500 rpm for 30 s. Second, a 1 M solution of prepared CuI in acetonitrile was coated on the PbI_2-coated films. Finally, the resulting thin films were heated at 200 °C.

2.2. γ-ray's irradiation

The γ-ray's exposure procedure of $CuPbI_3$ was carried out using a ^{60}Co (energy = 1.31 MeV and dose rate = 7.328 kGy/h) source in a closed chamber (Model SC220E, MDS Nordion). The γ-ray's exposure dose was changed from 0 to 75 kGy at room temperature in air.

2.3. Structural measurements

The crystalline size (D) and the microstrain (ε) of $CuPbI_3$ thin films before and after γ-ray's exposure were computed using the Debye–Scherer formula [24]:

$$D = \frac{0.94\lambda}{\beta \cos\theta} \tag{1}$$

$$\varepsilon = \frac{\beta \cos\theta}{4} \tag{2}$$

where 'λ = 1.5406 Å', is the incident X-ray wavelength, 'β' is the FWHM value, and 'θ' is the Bragg angle of the (002) diffraction peak.

The lattice constants of the hexagonal structure are determined using Millar indices of the (002) and (302) planes [24]:

$$\frac{1}{d^2} = \frac{4}{3}\left(\frac{h^2 + hk + k^2}{a^2}\right) + \frac{l^2}{c^2} \tag{3}$$

where '*d*' is the interplanar spacing, '*a* and *c*' are the lattice constants and '(*h*, *k*, *l*)' are the Millar indices of the plane.

2.4. Optical measurements

To calculate the band gap value (E_g) by using transmission and diffuse reflectance spectra, the absorption coefficient (α) is measured by applying Eqs (4) and (5), respectively [25]:

$$\alpha = \frac{1}{t}\ln\left(\frac{T}{100}\right) \tag{4}$$

$$F(R) = \frac{(1-R)^2}{2R}, \quad \alpha = \frac{F(R)}{t} \tag{5}$$

$$(\alpha h\nu) = \frac{F(R)h\nu}{t} = A(h\nu - E_g)^m \tag{6}$$

where 't' is the thickness of the $CuPbI_3$ film, 'T, R' represent transmission and reflectance, 'h' is the plank's constant, 'ν' is the frequency of electromagnetic waves, 'A' is a constant, and '$m = ½$' for direct allowed transition [25]. The estimated energy band gap of all samples was computed from the extrapolation of a straight part $(\alpha h\nu)^2$ vs. (hν) plot to the x–axis. The Urbach energy was computed through the ln(α) vs. (hν) plot.

The extinction coefficient (k), refractive index (n) and optical density (σ_{op}) of $CuPbI_3$ thin films before and after irradiation were measured using the following equations [26]:

$$k = \frac{\alpha\lambda}{4\pi} \tag{7}$$

$$n = \frac{(1+R)}{(1-R)} - \sqrt{\frac{4R}{(1-R)^2} - k^2} \tag{8}$$

$$\sigma_{op} = \frac{\alpha n c}{4\pi} \tag{9}$$

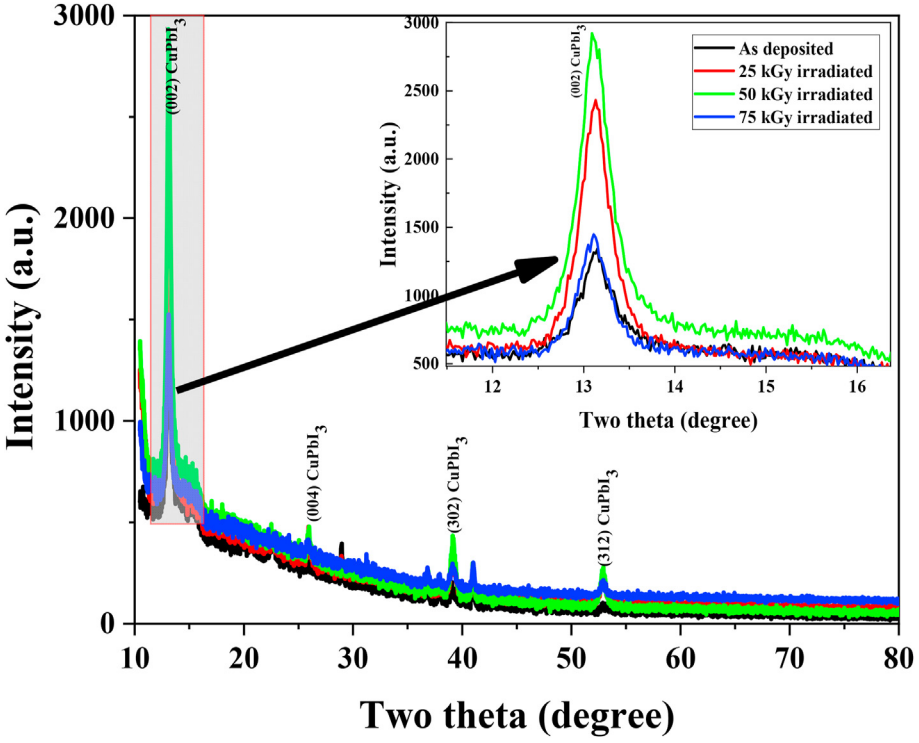

Fig. 1 – X-ray diffraction pattern of $CuPbI_3$ thin films with different γ-ray's irradiation doses.

where 'c' is the speed of light.

The dielectric parameters belong to the values of 'n' and 'k'. The following relations were used to estimate real and imaginary part of dielectric constants [26].

$$\varepsilon_r = n^2 - k^2 \tag{10}$$

$$\varepsilon_i = 2nk \tag{11}$$

where ε_r is the real part and ε_i is the imaginary part of the dielectric constant.

2.5. Electrical measurement

The dc conductivity (σ_{dc}) across the grain boundaries was determined from the grain boundary resistance using the following equation:

$$\sigma_{dc} = \frac{t}{AR} \tag{12}$$

where 'A' is the active area and 'R' is the grain boundary resistance.

2.6. Characterization

X-ray diffraction (XRD- Panalytical X'Pert 3) analysis of the as-deposited and γ-ray's -irradiated CuPbI3 thin films was carried out using CuKα R-rays. Surface morphology and electron dispersive X-ray measurements were observed by field emission scanning electron microscopy (FESEM) (JEOL). Transmission and diffuse reflectance spectra were obtained using a double beam and integrating sphere spectrophotometer (JASCO-V 670). A room-temperature photoluminescence (PL) study was performed by a spectro-fluorometer (JESCO FP-

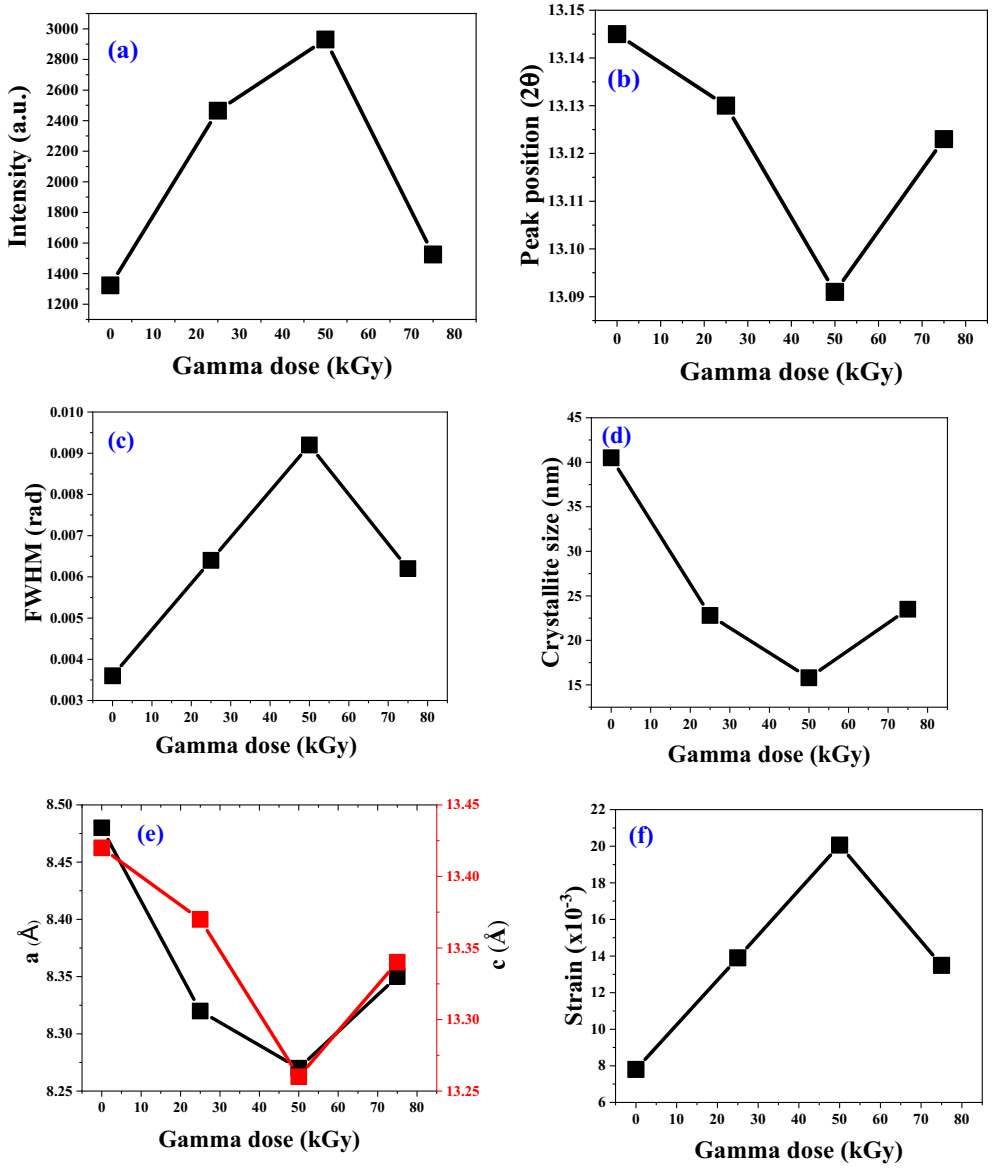

Fig. 2 – Variation in the structural parameters of $CuPbI_3$ thin films: (a) XRD peak intensity, (b) peak position, (c) full width at half maxima, (d) crystallite size, (e) lattice constants and (f) compression strain with γ-ray's irradiation dose.

8200). The electrical impedance of all samples was measured by an impedance analyzer and analyzed with z-view software.

3. Results and discussion

3.1. Structural investigation

The structural analysis of the $CuPbI_3$ thin film with and without γ-ray's exposure at different dosages characterized by XRD is shown in Fig. 1. The XRD peaks (002) (004) (302), and (312) positioned at 12.9, 25.7, 39.7, and 52.5, respectively, indicate the crystalline nature of the thin film. The XRD pattern confirmed the hexagonal structure of deposited $CuPbI_3$ thin films, which is in good agreement with published literature data in [27]. A significant modification was detected in the XRD structure of $CuPbI_3$ after exposure to different doses of γ-ray's, as depicted in the inset of Fig. 1. This effect indicates the $CuPbI_3$ response under irradiation at doses ranging from 0 kGy to 75 kGy.

With an increase in γ-ray's exposure doses, different changes took place on the $CuPbI_3$ crystal structure. The growth in the peak intensity with γ-ray's doses up to 50 kGy and then a decrease at 75 kGy were observed, as shown Fig. 2-a. This alteration in the XRD peak intensity can be attributed to nanostructure changes (crystals reorganizing themselves during exposure to γ-ray's radiation) of $CuPbI_3$ thin films. Shifting the peak position, irradiation introduces lattice imperfection into interstitial sites, which can be associated with the shifting of the XRD peak positions up to a certain dose level, as shown in Fig. 2-b [28]. There was an upsurge of FXHM with an increase in γ-ray's dose at a specific dose, and it then decreased, as shown in Fig. 2-c, due to the alteration in the crystallite size.

The crystallite size of $CuPbI_3$ thin films before and after γ-ray's irradiation with different doses can be measured by the FWHM of the XRD diffraction via Debye–Scherrer's formula [29]. The crystallite size decreased with increasing dose up to 50 kGy and then increased, as shown in Fig. 2-d. This behavior may be due to the formation of structural defects caused by the incident γ-ray's rays, which then lead to a reduction in the crystallite size [30]. Badawy et al. also reported the decreased of crystallite size of the rutile phase $ZnTiO_3$ after gamma irradiation with same dose level [31]. At a γ-ray's dose of 75 kGy, the increase in the crystallite size may be due to energy transferred from incident photons to the lattice, with the heating effects attributed to agglomeration in the grain boundaries.

Fig. 2-e shows the variation in lattice constant values of $CuPbI_3$ pre and post γ-ray's irradiation. This proves that the

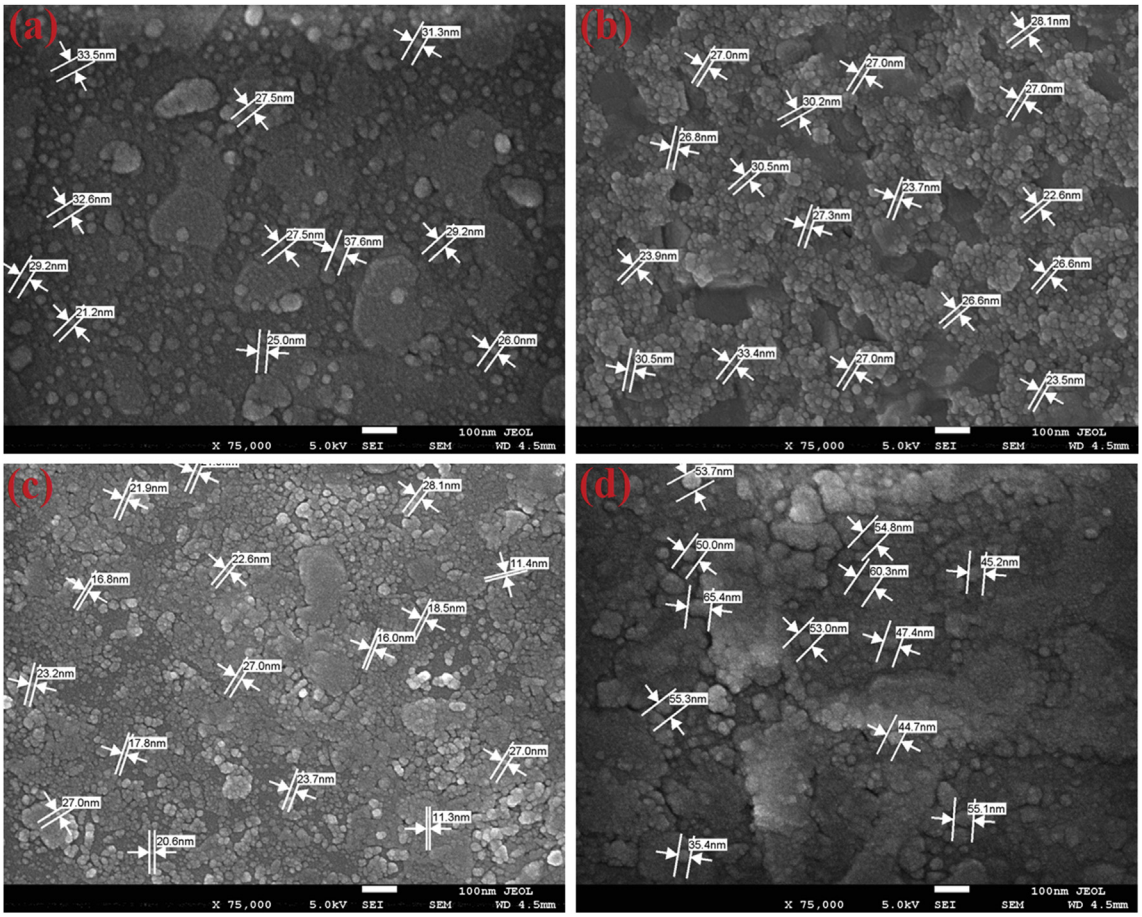

Fig. 3 – Morphology of (a) as-prepared, (b) 25 kGy, (c) 50 kGy, (d) 75 kGy irradiated, (e) EDS analysis and (f) cross section of $CuPbI_3$ thin films.

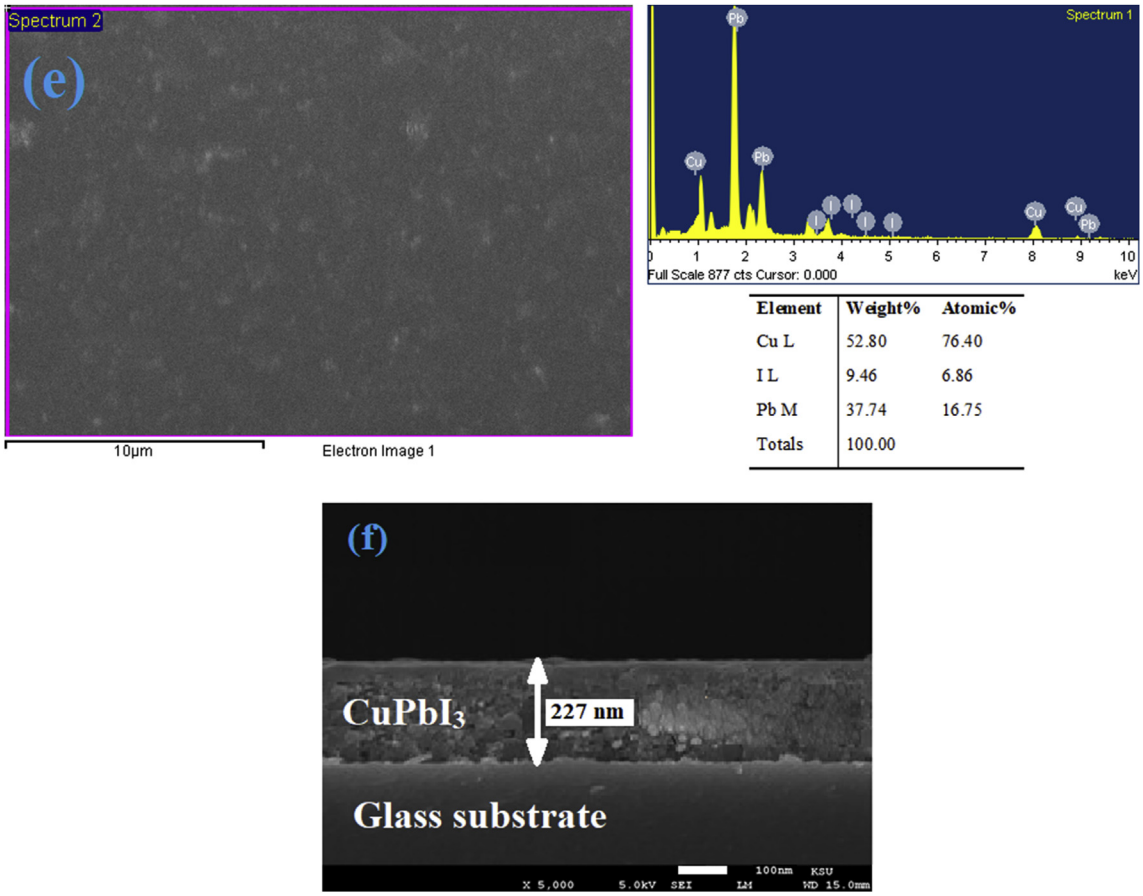

Fig. 3 – *(continued)*.

lattice constant values change with γ-ray's irradiation, similar to the trend of the crystallite size. This reduction in lattice parameters can be attributed to either the deviation in lattice vacancies in the thin films caused by the incident γ-ray's rays [32] or the formation of the compressive strain in irradiated thin films, which also appeared in the XRD peak expansion [33,34]. The compressive strain as a function of γ-ray's irradiation dose is represented in Fig. 2-f.

3.2. *Surface morphology*

The surface morphology of $CuPbI_3$ thin films pre and post exposure to different doses of γ-ray's rays is shown in Fig. 3a-d. The deposited FESEM image shows small closely packed granular-shaped grains dispersed completely on the surface of the substrate without any pinholes or cracks (Fig. 3-a). There was a significant alteration observed in the grain size and on the surface of γ-ray's-irradiated films, which meaningfully affected the γ-ray's irradiation dose. Fig. 3-b and c show that the surface of the irradiated samples contains small grains up to a 50-kGy γ-ray's dose, but they are not much more closely packed than the nonirradiated sample and have small voids. It is also detected that as γ-ray dose is increased, the grain size is decreased up to 50 kGy from 33 nm to 22 nm, this phenomenon is due to the grain splitting and the induced heat effect, generated by the incident γ-ray's [35]. However, with 75-kGr γ-ray's irradiation is increased as compared to the other samples, as indicated in Fig. 3-d, the surface of the thin films appears to be irregular and agglomerated, which reveal the change of crystallinity. So, we can say that the absorbed γ-ray's photons affect the microstructure in a different way which suggests that several physical interactions happened within the crystal lattice [36]. Wahab et al. have reported the variation grain size with gamma irradiated dose of ZnO nanorods [37]. Furthermore, EDX analysis was performed to measure the thin film composition of the as-deposited $CuPbI_3$, as shown in Fig. 3-e. The EDX spectra confirm the atomic and weight percentages of Cu, Pb, and I elemental compositions of the prepared $CuPbI_3$. The thickness of the prepared $CuPbI_3$ thin films is estimated from the cross-sectional FESEM image, as shown in Fig. 3-f, and can be found to be 227 nm.

3.3. *Optical analysis*

Fig. 4 a and b depict the transmission and diffuse reflectance spectra of the $CuPbI_3$ thin film before and after exposure to different γ-ray's ray doses, respectively. The transmission and reflectance of thin films have the same trend of variation as found in earlier characterizations (FESEM and XRD). The band edge in the transmission spectra is showed the red shift to

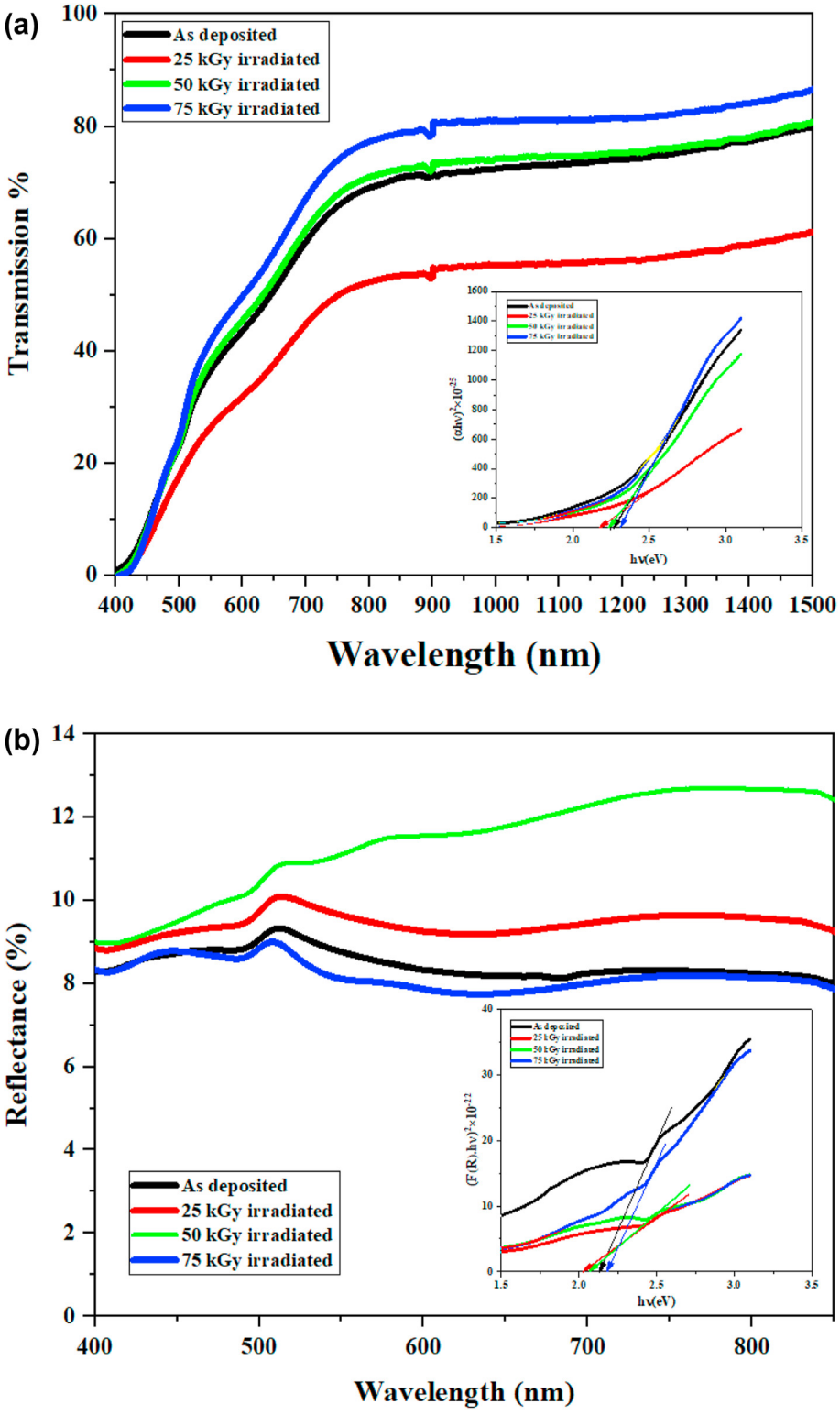

Fig. 4 – (a) Transmittance spectra (inset) Tauc's plot for band gap from transmission (b) Reflectance spectra (inset) Tauc's plot for band gap from reflectance of $CuPbI_3$ thin films at different γ-ray's irradiation doses.

50 kGy and then shifts back at higher doses. The optical band gap (E_g) is an imperative feature for different applications of nanoscale thin films. UV–Vis transmission and diffuse reflectance spectra were used to determine the band gap values of $CuPbI_3$ thin films before and after γ-ray's exposure using Eq. (6).

The energy band gap values of $CuPbI_3$ with and without γ-ray's exposure from the above equation are computed. The band gap is found by a linear portion of the plot to the x-axis at 0 from Tauc's plot $((\alpha h\nu)^2$ vs $h\nu)$, as depicted in the inset of Fig. 4 a and b. The band gap values increased with increasing γ-ray's dose from 0 to 50 kGy and then decreased at 75 kGy. The measured values of band gaps of all samples from transmission and reflectance are given in Table 1. The changes in the band gap energies were due to variations in grain size [24]. The correlation between the band gap and grain size can be made for all γ-ray's doses. The reduction in grain size was linked to an increase in the band gap. The trend of band gap with dose suggests the use of $CuPbI_3$ thin films as a gamma dosimeter. The band gap variation is attributed to radiation-induced defects and induced defect density, which may shift the absorption edge. After irradiation the defects density levels in conduction and valence bands have been depending on the irradiation dose level. Therefore, the incident γ-rays significantly change the electronic energy states in the targeted materials [38]. Senthil et al. reported the same results for γ-ray's-irradiated SnO thin films [39].

The optical properties of $CuPbI_3$ are intensely influenced by the presence of a localized energy state near the forbidden band gap. The Urbach energy gives appreciated evidence concerning the defect states that represent imperfections in the deposited thin films. Hence, absorption edges for Urbach energy are generally presented below the forbidden energy band gaps. The value of Urbach energy was measured by the gradient of the linear part of $\ln(\alpha)$ vs. $h\nu$ plots, as shown in Fig. 5-a. The Urbach energy values were considerably increased after γ-ray's exposure at 25 kGy and then decreased with increasing γ-ray's irradiation dose. The decrease in Urbach energy after 25 kGy may be due to the reduction of the defect density near the band edges and a relaxation of the distorted structure. Deviations of the extinction coefficient (k) as a function of wavelength with and without γ-ray's irradiation at different doses are presented in Fig. 5-b. The increases and decreases in the extinction coefficient are associated with light absorption at different wavelengths. In the case of perovskite thin films, additional absorption arises in the grain boundaries, which leads to the absorption edge of the extinction coefficient against wavelengths lower than the fundamental absorption edge in the transmission spectra.

The variation of refractive index (n) with wavelength for $CuPbI_3$ thin films before and after γ-ray's irradiation is depicted in Fig. 6-a. All samples had a well-defined maximum, and the peak values of the refractive index increased at 25 kGy and then reduced with an additional rise in the γ-ray's dose. These changes are related to the structural variation of thin films with γ-ray's dose [40,41]. Fig. 6-b shows the optical density of the as-deposited and γ-ray's-irradiated $CuPbI_3$ thin films as a function of photon energy. It is generally dependent on the absorption coefficient values of thin films [42]. The optical conductivity is found to be enhanced after the initial dose and then reduced with increasing γ-ray's dose.

The electron transition in semiconductor thin films is associated with the dielectric parameters as a function of dependence. The real and imaginary parts of dielectric parameters are linked to the decrease of the speed of light in the thin films and light absorption in the dipole movement, respectively. The real and imaginary dielectric constants are influenced by the refractive index and extinction coefficient of thin films. The values of real and imaginary dielectric parameters as a function of wavelength are increased at certain γ-ray's doses and then reduced gradually with the increase of, as shown in Fig. 7- (a & b). The minimum values of dialectic

Table 1 – Optical parameters of $CuPbI_3$ thin films at different γ-ray's irradiation doses.

γ-ray's dose (kGy)	Band gap 'E_g' (eV)		Urbach Energy (eV)	Minimum value Extinction coefficient (k)	Refractive index (n) at 515 nm	Minimum value Optical conductivity ($\times 10^{14}$)	Dielectric constant (ε) at 515 nm	
	By Transmission	By Reflectance					Real	Imaginary
0	2.23	2.03	0.99	0.12	2.04	3.6	0.99	4.13
25	2.31	2.12	0.53	0.26	2.36	9.52	1.30	5.53
50	2.38	2.21	1.08	0.11	2.13	4.25	1.03	4.54
75	2.26	2.18	1.22	0.07	2.32	2.58	1.11	5.34

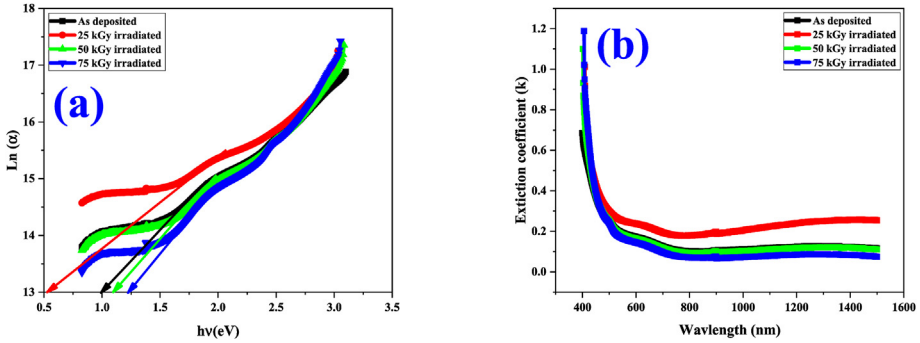

Fig. 5 – (a) Urbach energy and (b) extinction coefficient of $CuPbI_3$ thin films at various γ-ray's irradiation doses.

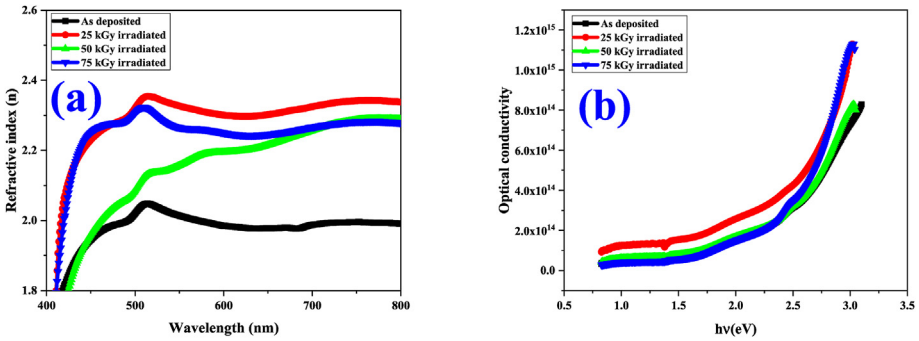

Fig. 6 – (a) Refractive index and (b) optical conductivity of $CuPbI_3$ thin films at different γ-ray's irradiation doses.

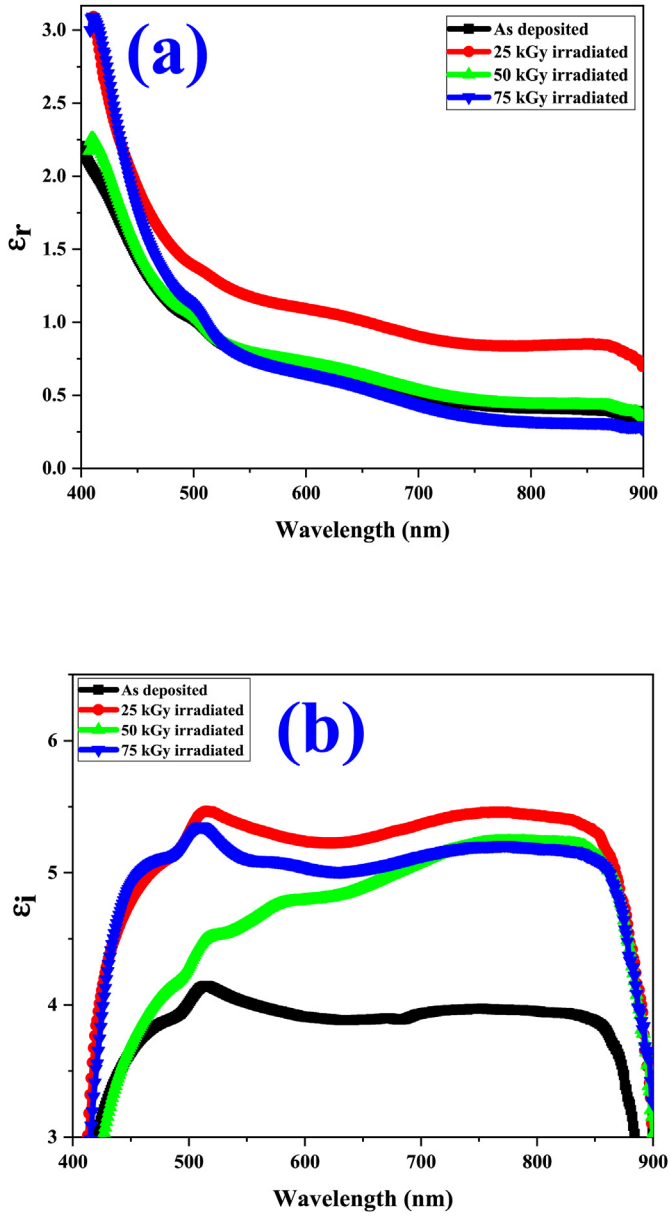

Fig. 7 – (a) Real and (b) imaginary parts of the dielectric constant of $CuPbI_3$ thin films at different γ-ray's irradiation doses.

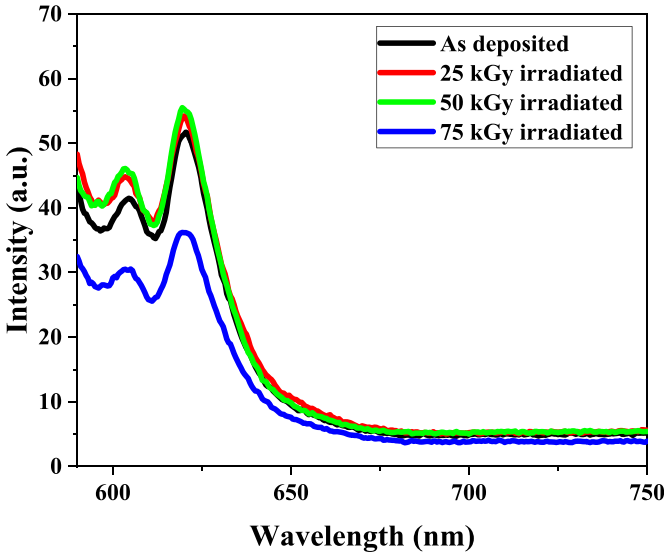

Fig. 8 – Photoluminescence spectra of $CuPbI_3$ thin films at different γ-ray's irradiation doses.

parameters are accredited to faster passage of electromagnetic radiation within the nonradiated and irradiated thin films [43].

3.4. *Photoluminescence study (PL)*

To inspect the impact of γ-ray's irradiation on the luminescence properties, room-temperature PL spectra of the $CuPbI_3$ thin films under 0- to 75-kGy γ-ray's doses are displayed in Fig. 8 at an excitation wavelength of 585 nm. The main transition peak at 620.35 nm is considered to be related to the conduction-to-valance band transition for all samples. Furthermore, a weak emission peak at a wavelength of 606.3 nm was observed. This emission PL peak has been attributed to structural imperfection, which is high photon γ-ray's irradiation [44]. The intensity of the main PL peak is improved under γ-ray's ray doses of 0–50 kGy. This occurrence is due to the surface ionization defect density on the surface of thin films [45]. As reflected, the as-deposited $CuPbI_3$ thin film has certain nonradiative recombination centers through photoluminescence excitation. An irradiation dose of up to 50 kGy may induce an internal strain that is predictable to not only release the present trap but also correspondingly generate additional new defects near the band edge, which is important to improve the PL intensity [44]. Similar results of the PL intensity enhancement were also found by [46] when the GaAs thin films were irradiated by low-dose γ-rays. The γ-ray's irradiation dose level is very important for the luminescence of thin films. At a high dose level of approximately 75 kGy, the PL intensity decreased due to the created deep-

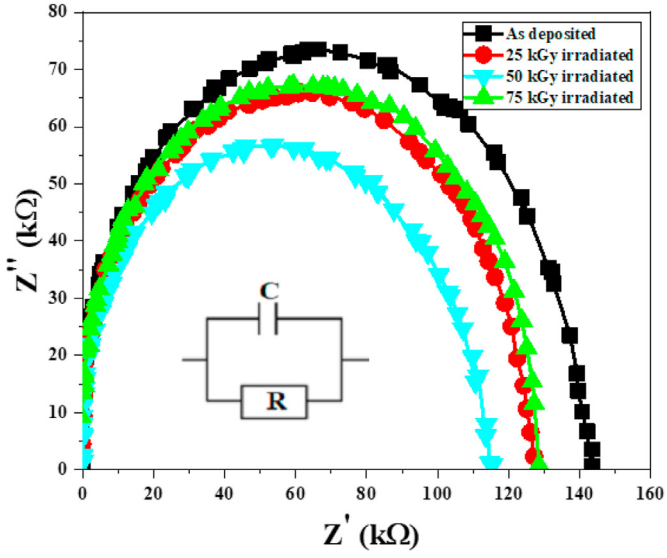

Fig. 9 – Nyquist plot of $CuPbI_3$ thin films at different γ-ray's irradiation doses along with equivalent circuits after fitting impedance spectroscopy data.

Table 2 – Electrical parameters of $CuPbI_3$ thin films at different γ-ray's irradiation doses eliminated from impedance spectroscopy.

γ-ray's Dose (kGy)	R (kΩ)	C ($\times 10^{-9}$ F)	σ_{dc} ($\times 10^{-10}$ S/m)
0	142	65	6.47
25	128	68	7.19
50	114	64	8.10
75	129	66	7.13

level defects in the thin films [47]. These effects may have indicated that γ-ray's irradiation modified the structure of $CuPbI_3$ thin films, as determined by XRD analysis.

3.5. *Electrical impedance spectroscopy*

To understand the γ-ray's irradiation dose effects and internal electoral charge transport process, electrical impedance spectroscopy (EIS) is an appropriate technique. Fig. 9 demonstrates the Nyquist plots of $CuPbI_3$ thin films before and after γ-ray's irradiation at different doses. The EIS results were fitted with Z-View corresponding to the equivalent RC parallel circuit, linked with the charge transformation between the grain boundaries in nanocrystal $CuPbI_3$ thin films, as depicted in the inset of Fig. 9 [48,49]. The grain boundary resistance (R) of the as-deposited and γ-ray's-irradiated samples was measured from the intercept value of the semicircle with the Z′-axis. It can be seen clearly that the grain boundary resistance gradually decreased with increasing γ-ray's dose, indicating the tremendous traps induced by γ-ray's irradiation. In contrast, the grain boundary resistance R indicates the reverse trend, becoming greater at the 75 kGy γ-ray's ray dose. The reduction of grain boundary resistance has a main concern with the enhancement in the crystallinity thin film, as well as the growth in the grain boundary resistance might be associated with the improvement of charge carrier density. The reduction of grain boundary at 75 kGy might be attributed to the decreased capture of charges at grain boundaries by eradication of the structural defects after γ-ray's irradiation. The calculated value of the grain boundary capacitance (C) is found to be almost identical for all samples of $CuPbI_3$ thin films. By using the designated fitting RC parallel equivalent circuit, the appropriate grain boundary resistance and capacitance at different γ-ray's exposure doses were measured and are given in Table 2.

The value of dc conductivity rises with γ-ray's irradiation doses for dose value of 50 kGy of γ-rays. The dc conductivity is observed to decline upon irradiation to higher γ doses (75 kGy). As compared to the as deposited thin film, there is an overall improvement dc conductivity upon γ-ray irradiation due to the free charge carrier concentration induced by γ-ray's radiation [50]. The increase in DC conductivity at room temperature indicates that their mobility also increased with γ-ray's irradiation and that irradiation contributed to charge carrier transportation in the $CuPbI_3$ thin films [51]. Swaroop et al. was investigate the similar trend of increasing dc conductivity with gamma irradiation dose at room temperatures [52].

4. Conclusion

XRD results reveal that the crystalline size decreases from 41 to 16 nm with γ-ray's dose at 50 KGy for the $CuPbI_3$ films. Structural properties illustrated that the crystalline nature of the as-prepared sample enhanced up to a 50-kGy γ-ray's ray dose with a preferred orientation (002) and then reduced with more increasing γ-ray's ray dose. The FESEM results showed the alterations in the surface morphology of the $CuPbI_3$ subsequently increasing with γ-ray's ray doses. At a dose of 75 kGy, the surface appeared irregular and agglomerated. The transmission and reflectance of the thin film increased at 25 and 50 kGy and then decreased. A slight variation in the band gap was detected in the same dose range due to the quantum confinement effect generated by γ-ray's irradiation. Enhancement of the PL intensity of $CuPbI_3$ thin films for γ-ray's doses of 0–50 kGy was noticed. Impedance spectroscopy analysis explained that the grain boundaries capacitance was almost the same for all γ-ray's ray doses. However, the grain resistance decreased and the grain conductivity increased with the γ-ray's dose. All of these properties indicate that $CuPbI_3$ thin films exposed at 50 kGy are more crystalline and have large optical reflectance and transmission, excellent optical parameters and high conductivity.

Declaration of Competing Interest

The authors declare that they have no known competing financial interest or personal relationships that could have appeared to influence the work reported in this manuscript.

Acknowledgments

The authors would like to extend their sincere appreciation to the Deanship of Scientific Research at King Saud University for funding under Research Group No. RG-1441-315.

REFERENCES

[1] Abdelhady AL, Saidaminov MI, Murali B, Adinolfi V, Voznyy O, Katsiev K. Heterovalent dopant incorporation for bandgap and type engineering of perovskite crystals. J Phys Chem Lett 2016;7:295–301.
[2] Baikie T, Fang Y, Kadro JM, Schreyer M, Wei F, Mhaisalkar SG. Synthesis and crystal chemistry of the hybrid perovskite (CH3NH3) PbI3 for solid-state sensitised solar cell applications. J Mater Chem A 2013;1:5628–41.
[3] Birowosuto MD, Cortecchia D, Drozdowski W, Brylew K, Lachmanski W, Bruno A. X-ray scintillation in lead halide perovskite crystals. Sci Rep 2016;6:37254.
[4] Boyd CC, Cheacharoen R, Leijtens T, McGehee MD. Understanding degradation mechanisms and improving stability of perovskite photovoltaics. Chem Rev 2019;119:3418–51.

[5] Saeed M, Ali MA, Murad S, Ullah R, Alshahrani T, Laref A, et al. Pressure induced structural, electronic, optical and thermal properties of CsYbBr3, a theoretical investigation. J Mat Res Technol 2021;10:687–96.
[6] Ullah R, Reshak AH, Ali MA, Khan A, Murtaza G, AL-Anazy M, et al. Pressure-dependent elasto-mechanical stability and thermoelectric properties of MYbF3(M = Rb, Cs) materials for renewable energy. Int J Energy Res 2021;45:8711–23.
[7] Ali MA, Ullah R, Dar SA, Murtaza G, Khan A, Mahmood A. Modeling of structural, elastic, mechanical, acoustical, electronic and thermodynamic properties of XPdF3 (X = Rb, Tl) perovskites through density functional theory. Phys Scripta 2020;95:075705.
[8] Ali MA, Zarin H, Salam S, Shah A, Dar SA, Khan A, et al. DFT investigations of structural, magnetic, electronic, and optical properties of CsEuCl3. J Supercond Nov Magnetism 2020;33:1045–105.
[9] Ali MA, Ullah R, Murad S, Dar S,A, Khan A, Murtaza G, et al. Insight into pressure tunable structural, electronic and optical properties of CsYbF3 via DFT calculations. Eur. Phys. J. Plus 2020;135:309.
[10] Knoll GF. Radiation detection and measurement. 4th ed. New York: Wiley; 2011.
[11] Starkenburg DJ, Johns PM, Baciak JE, Nino JC, Xue J. J Appl Phys 2017;122:225502.
[12] Stoumpos CC, Malliakas CD, Peters JA, Liu Z, Sebastian M, Im J, et al. Crystal growth of the perovskite semiconductor CsPbBr3: a new material for high-energy radiation detection. Cryst Growth Des 2013;13:2722–7.
[13] Lia CL, Hana C, Zhangb YB, Zanga ZG, Wanga M, Tanga XS, et al. Enhanced photoresponse of self-powered perovskite photodetector based on ZnO nanoparticles decorated CsPbBr3 films. Sol Energy Mater Sol Cells 2017;172:341–6.
[14] Han C, Li CL, Zang ZG, Wang M, Sun K, Tanga XS, et al. Tunable luminescent CsPb2Br5 nanoplatelets: applications in light-emitting diodes and photodetectors. Photon Res 2017;5:473–80.
[15] Ramasamy P, Lim DH, Kim B, Lee SH, Lee MS, Lee JS. All-inorganic cesium lead halide perovskite nanocrystals for photodetector applications. Chem Commun 2016;52:2067–70.
[16] Wu Y, Han D, Chakoumakos BC, Shi H, Chen S, Du Mao-Hua, et al. Zero-dimensional Cs4EuX6 (X = Br, I) all-inorganic perovskite single crystals for gamma-ray spectroscopy. J Mater Chem C 2018;6:6647.
[17] Hany I, Yang G, Phan QV, Kim HJ. Thallium lead iodide (TlPbI3) single crystal inorganic perovskite: electrical and optical characterization for gamma radiation detection. Mater Sci Semicond Process 2021;121:105392.
[18] He Y, Matei L, Jung HJ, McCall KM, Chen M, Stoumpos CC, et al. High spectral resolution of gamma-rays at room temperature by perovskite CsPbBr3 single crystals. Nat Commun 2018;9:1609.
[19] Chung I, Song JH, Im J, Androulakis J, Malliakas CD, Li H, et al. J Am Chem Soc 2012;134:8579.
[20] Darwish A, Issa SA. Variation in the structure and optical properties of gamma-irradiated Vanadyl 2,3-naphthalocyanine (VONc) nanostructure films, Radiat. Phys Chem 2018;148:100–5.
[21] Zeyada H, Makhlouf M, El-Nahass M. Influence of gamma ray irradiation and an-nealing temperature on the optical constants and spectral dispersion parameters of metal-free and zinc tetraphenylporphyrin thin films: a comparative study. Spectrochim Acta A Mol Biomol Spectrosc 2015;148:338–47.
[22] Arshak K, Korostynska O, Harris J, Morris D, Arshak A, Jafer E. Thin Solid Films 2008;516:1493–8.
[23] Holmes-Siedle AG, Adams L. Handbook of radiation effects. Oxford, New York: OxfordUniversity Press; 1993.
[24] Ali SM. J Mater Sci Mater Electron 2017;28:16314.
[25] Ejderha K, Yildirim N, Turat A. Superlattice Microst 2010;47:241.
[26] Thomas R, Mathavan T, Ganesh V, Yahia IS, Zahran HY, AlFiafy S. Investigation of erbium co-doping on fluorine doped tin oxide via nebulizer spray pyrolysis for optoelectronic applications. Opt Quant Electron 2020;52:248.
[27] Sookhakian M, Mumtaz A, Mazhar M. Photoelectrochemical water splitting over mesoporous CuPbI3 films prepared by electrophoretic technique. Monatsh Chem 2017;148:981–9.
[28] Kuku TA. Ionic transport and galvanic cell discharge characteristics of CuPbI3thin films. Thin Solid Films 1998;325:246.
[29] Heavens OS. Optical properties of thin solid films. New York: Dover; 1991.
[30] Sudha A, Maity TK, Sharma SL. Mater Lett 2016;164:372.
[31] Badawy AA, El-Shafey SE, Abd El All S, El-Shobaky GA. Effect of γ-irradiation and calcination temperature of nanosized ZnO/TiO2 system on its structural and electrical properties. Advances in Chemistry 2014:301410.
[32] Tawfik A, Hamada IM, Hemeda OM. Effect of Laser irradiation on the structure and electromechanical properties of Co–Zn ferrite. J Magn Magn Mater 2002;250:77–82.
[33] Dogra A, Singh M, Kumar R. Mössbauer studies of 190 MeV Af ion irradiated NiMn0.05TixMgxFe1.95–2xO4 ferrite. Nucl Instrum Methods B 2003;207:296.
[34] Angadi B, Jali VM, Lagare MT, Kini NS, Umarji AM, Kumar R, et al. 50 MeV Li3+ irradiation effects on the thermal expansion of Ca1–xSrxZr4P6 O24. Nucl Instrum Methods B 2002;187:87.
[35] Ranwa S, Barala SS, Fanetti M, Kumar M. Effect of gamma irradiation on Schottky-contacted vertically aligned ZnO nanorod-based hydrogen sensor. Nanotechnology 2016;27(34):345502.
[36] Al-Hamdani NA, Al-Alawy RD, Hassan SJ. Effect of gamma irradiation in the structural and optical properties of ZnO thin films. J. Comput. Eng. 2014;16:11–6.
[37] Wahab HA, Salama AA, El-Saeid AA, Nur O, Willander M, Battisha IK. Optical, structural and morphological studies of (ZnO) nano-rod thin films for biosensor applications using sol gel technique. Results Phys 2013;3:46–51.
[38] Souli M, Nefzi C, Seboui Z, Mejri A, Vidu R, Turki NK. Improved structural properties, morphological and optical behaviors of sprayed Cu2ZnSnS4thinfilms induced by high gamma radiations for solar cells. Mater Sci Semicond Process 2018;83:50–7.
[39] Senthil Srinivasan VS, Patra MK, Choudhary VS, Pandya A. Gamma irradiation study of tin oxide thin films for dosimetrist applications. J Optoelectron Adv Mater 2007;9(12):3725–8.
[40] Yamaguchi K, Nakayama N, Matsumoto H, Ikegami S. Jpn J Appl Phys 1977;16:1203.
[41] Tepehan F, Ozer N. Sol. En. Mater. Sol. Cells 1993;30:353.
[42] Mazloom J, Ghodsi FE, Gholami M. Fiber-like stripe ATO (SnO2:Sb) nanostructured thin flms grown by sol–gel method: optical, topographical and electrical properties. J Alloys Compd 2013;579:384–93.
[43] Hassanien AS. Studies on dielectric properties, opto-electrical parameters and electronic polarizability of thermally evaporated amorphous Cd50S50-xSex thin flms. J Alloys Compd 2016;671:566–78.
[44] Yang TY, Gregori G, Pellet N, Grätzel M, Maier J. The significance of ion conduction in a hybrid organic-inorganic

lead-iodide-based perovskite photosensitizer. Angew Chem Int Ed 2015;127:8016–21.
[45] Cui Y, Shao X, Prada S, Giordano L, Pacchioni G, Freund HJ, et al. Surface defects and their impact on the electronic structure of Mo-doped CaO films: an STM and DFT study. Phys Chem Chem Phys 2014;16:12764–72.
[46] Borkovskaya OY, Dmitruk NL, Litovchenko VG, Mishchuk ON. Model of the radiation-stimulated ordering effect in III-V semiconductors. Sov Phys Semiconduct 1989;23:129–32.
[47] Borkovskaya OY, Dmitruk NL, Konakova RV, Litovchenko VG, Tkhorik YA, Shakhovtsov VI. Effect of the interface on radiation defect formation in Gallium Arsenide. Radiat Eff 1979;42:249–51.
[48] Gopel W, Schierbaum KD. Sens Actuators B 1995;1:26–7.
[49] Yang MR, Chu SY, Chand RC. Sens Actuators B 2007;122:269.
[50] Arof AK, Amirudin S, Yusof SZ, Noor IM. Phys Chem Chem Phys 2014;16:1856–67.
[51] N. M. AL-Hada, A. M. AL-Ghaili, H. Kasim, M. A. Saleh, E. Saion, J. Liu, W. Jihua, Synthesis and characterization of conducting polyaniline based on ANI-PVA-MgCl2 composites using gamma radiation technique, Digital Object Identifier https://doi.org/10.1109/ACCESS.2020.3012730.
[52] K. Swaroop, C. S. Naveen, H. S. Jayanna, H. M. Somashekarappa, Effect of gamma irradiation on dc electrical conductivity of ZnO nanoparticles . Solid State Phys: AIP Conf. Proc. 1665, 050100-1–050100-3; https://doi.org/10.1063/1.4917741.